MAGNETIC RESONANCE IN CHEMISTRY
Magn. Reson. Chem. 2001; **39**: S149–S157

Stray field gradient NMR reveals effects of hydrogen bonding on diffusion coefficients of pyridine in mesoporous silica

E. Gedat,[1] A. Schreiber,[2] G. H. Findenegg,[2] I. Shenderovich,[1] H.-H. Limbach[1] and G. Buntkowsky[1]*

[1] Freie Universität Berlin, Institut für Chemie, Takustrasse 3, 14195 Berlin, Germany
[2] Technische Universität Berlin, Iwan-N.-Stranski-Laboratorium für Physikalische und Theoretische Chemie, Strasse des 17. Juni 112, 10623 Berlin, Germany

Received 18 July 2001; Revised 31 August 2001; Accepted 4 September 2001

The diffusion of pyridine confined in mesoporous silica MCM-41 (d_{pore} = 3.3 nm) was studied with stray field gradient (SFG) NMR diffusometry as a function of the filling factor of the mesopores at room temperature, employing a laboratory-built SFG setup. The translational diffusion of pyridine in MCM-41 is found to be anisotropic and the diffusion parallel to the pores' cylinder axes is much faster than that perpendicular to them. The parallel diffusion coefficient depends strongly on the filling level of the guest liquid inside the pores. For a filling level of 25%, which corresponds approximately to a monomolecular layer of pyridine molecules hydrogen bonded to surface — SiOH groups, a parallel diffusion coefficient of $D_{||} = 1.0 \times 10^{-9}$ m^2 s^{-1} is found, which is slower than the diffusion coefficient of the bulk liquid ($D = 1.6 \times 10^{-9}$ m^2 s^{-1}). For higher filling factors the parallel diffusion coefficient increases and at a filling factor of 85% a diffusion coefficient of $D_{||} = 6.8 \times 10^{-9}$ m^2 s^{-1} is reached. The perpendicular diffusion coefficient of $D_{\perp} = 3.7 \pm 2.0 \times 10^{-11}$ m^2 s^{-1} is independent of the filling factor. Employing additional ^{15}N MAS data for the pyridine inside the mesopores, a microscopic model of the diffusion is proposed, which depends on the exchange of the slowly diffusing hydrogen-bonded surface pyridine molecules with fast-diffusing free pyridine molecules inside the pores. Copyright © 2001 John Wiley & Sons, Ltd.

KEYWORDS: NMR; stray field gradient NMR; hydrogen bonding; diffusion; pyridine; mesoporous silica; MCM-41

INTRODUCTION

While the effects of hydrogen bonding on molecular and intermolecular structures are well characterized by NMR spectroscopy, it is surprising that it was realized only recently that hydrogen bonding can also have drastic effects on diffusion rates, as revealed by gradient NMR spectroscopy.[1–3] The main reason why these effects have so long been neglected probably originates from the fact that for most diffusing systems the surface to volume ratio of the pores is so small that molecules in direct contact with the surface are only a minor percentage of the overall molecules inside the pores and thus the diffusion restrictions imposed on these molecules by hydrogen bonding are of only minor importance. However, with the recent developments of mesoscopically structured porous silica this is no longer true. These materials are characterized by pores with diameters in the range 2–50 nm[4] and have very large surface to volume ratios. Owing to their wide range of pore sizes they are very versatile molecular sieves. Moreover, they are interesting model systems for the study of surface–liquid and surface–solid interactions. Examples of this class of mesoporous silica materials are MCM-41[5] and SBA-15,[6] which are both characterized by a hexagonal ordered array of cylindrical pores. The diameter of the pores are determined by the preparation of the materials. They are in the range 2–6 nm for MCM-41 and 5–10 nm for SBA-15. The particle size is typically in the region of 5 μm. The pore to pore distance, which is estimated as the inverse length of the scattering vector in x-ray diffraction, is about 20% larger than the pore diameter. Owing to their high pore density and small pore diameters, their surface to volume ratio has a very high value.

The geometry of the pores is highly anisotropic, such that a preferred axis exists in the direction of the pores' cylinder axis, and diffusion of guest liquids in the pores is expected to exhibit deviations from ordinary diffusion.[7,8] In general, diffusion processes in porous media depend strongly on the type of the host and of the guest molecules. As a result of this dependence, different diffusion models for liquids and liquid guests in porous materials are discussed in the literature for various systems: ordinary diffusion,[9,10] restricted

*Correspondence to: G. Buntkowsky, Laboratory of Chemical Physics, NIDDK, National Institutes of Health, Building 5, Bethesda, Maryland 20892, USA. E-mail: bunt@chemie.fu-berlin.de
Contract/grant sponsor: Deutsche Forschungsgemeinschaft.

DOI: 10.1002/mrc.932

diffusion,[11,12] anisotropic diffusion[13,14] and diffusion of different phases with individual diffusion coefficients.[15] Ordinary diffusion is well known and describes the behavior of isotropic systems such as bulk liquids. Restricted diffusion was developed for unordered porous systems that are believed to exhibit a fractal structure, where the pore walls hinder free diffusion of the guest molecules. The time dependence of this type of diffusion is described by a power law. Anisotropic diffusion has been studied by NMR for various systems, e.g. water between lamellar layers of a liquid crystal,[13], salt water ice[16] and water in MCM-41.[14] The basic model of anisotropic diffusion is the existence of spatial directions where diffusion is much easier than in other spatial directions. Another possible scenario is a multiphase model for the diffusion of guest molecules, where the diffusion coefficients depend on the distance of the guest molecules from the surface, similar to the velocity profile of a laminar flow. Indications for such a behavior are found for example in protein water solutions,[11,17–22] where a phase of non-freezable water in the hydration shell of the protein co-exists with a phase of freezable bulk water. In the pores it may be possible to discriminate a phase attached to the surface and another phase in the pore volume. For resolving both phases in an experiment, however, it is necessary that the exchange between the both is slow on the time-scale of the experiment.

Owing to their surface—SiOH groups, mesoporous silicas are capable of forming hydrogen bonds to guest molecules. These guest molecules can act as proton acceptors in a hydrogen bond. Pyridine is a typical example of such a guest molecule. Here the endocyclic nitrogen acts as the proton acceptor. Thus, pyridine inside the pores of ordered silica is expected to form hydrogen bonds to the surfaces of the pores, which should be revealed as a change in the diffusion rate of the pyridine guest molecules. Comparing the diameter of a pyridine molecule of ~0.50 nm[23] with the diameters of the pores, it is evident that in these materials a large proportion of the pyridine molecules are in contact with the surface and thus are able to form hydrogen bonds.

In this work, the diffusion of pyridine as a guest molecule inside mesoporous MCM-41 was studied with stray field gradient (SFG) NMR[24–30] for different filling factors of the pyridine, ranging from a monomolecular layer of pyridine on the inner surfaces of the pores to nearly completely filled pores. The resulting diffusion data were analyzed according to the models described above and the influence of the hydrogen bonding on the diffusion was elucidated from these data.

The rest of this paper is organized as follows: first, after a short introduction into the necessary background of diffusion and gradient NMR, the Experimental section describes the synthesis and characterization of the MCM-41 material, the NMR sample preparation and our laboratory-built experimental SFG set-up. Next the experimental results for pyridine as guest molecule in the mesoporous silica MCM-41 are presented and discussed, and finally summarized in the conclusion section.

THEORETICAL BACKGROUND

The basics of stray field gradient NMR diffusometry are well known[11] and only some salient facts will be summarized here, which are necessary for the evaluation of the experimental data and in particular for the adaptation of the model of anisotropic diffusion in PFG experiments to SFG experiments.

A linear gradient $G = \partial B_0/\partial z$ of the main magnetic field $\mathbf{B}_0 = (0, 0, B_0)$ in the z-direction encodes the z-position of a spin as a position dependent Larmor-frequency $\omega_L = \gamma(B_0 + \mathbf{G} \cdot \mathbf{z})$, where γ is the gyromagnetic ratio of the nucleus under observation. If the spin is subject to a diffusion process this Larmor frequency becomes time dependent. This time dependence can be analyzed by the stimulated echo pulse sequence $\left[\left(\frac{\pi}{2}\right)_{\varphi_1} - \tau_1 - \left(\frac{\pi}{2}\right)_{\varphi_2} - \tau_2 - \left(\frac{\pi}{2}\right)_{\varphi_3} - \tau_1 - echo\right]$ (φ_1, φ_2, φ_3 are pulse phases which are phase cycled to remove pulse imperfections; see Table 1). After the initial 90° pulse the spins precess for a duration τ_1 with the Larmor frequency corresponding to their initial position. The value of τ_1 is selected to be short compared with the time-scale of the diffusion, so that diffusion processes during τ_1 are negligible. The second 90° pulse flips the spins back into the z-direction. After a waiting time τ_2, the third 90° pulse flips the spins back in the transversal plane. If the position of the spins and thus their Larmor frequency have not changed during the time τ_2, an echo is formed after the time τ_1 that has maximum intensity. If, however, the individual frequency of some spins has changed due to a diffusion process, the intensity of the echo is attenuated. Under macroscopic stationary conditions no flow is present, and the displacement of molecules is governed by diffusion. Thus, the attenuation of the amplitude $A(\tau_1, \tau_2, D)$ of the stimulated echo is a measure for diffusion processes of the observed spin ensemble. In addition to the diffusion process the echo attenuation is also dependent on T_1 (spin–lattice, longitudinal) and T_2 (spin–spin, transversal) relaxation processes.

For a quantitative evaluation of the echo decay $A(\tau_1, \tau_2, D)$ curves, the spin phase shift $\phi(t) = \gamma \int_0^t G(t')[z(t') - z(0)]dt'$ from position $z(0)$ to $z(t)$ has to be integrated over all molecules.

The echo attenuation for a Gaussian displacement distribution is $A_{diff} = \exp(-\frac{1}{2} < \phi^2(t) >)$, and thus the echo attenuation factor for ordinary diffusion with the stimulated

Table 1. Phase cycle for the three-pulse stimulated echo pulse sequence. Shown are the phases of the three pulses: PLS1 for the first pulse, PLS2 for the second and third pulse, and RLS for the receiver phase

PLS1	$+X$	$+X$	$+X$	$+X$	$+Y$	$+Y$	$+Y$	$+Y$	$-X$	$-X$	$-X$	$-X$	$-Y$	$-Y$	$-Y$	$-Y$
PLS2	$+Y$	$-X$	$-Y$	$+X$	$-X$	$-Y$	$+X$	$+Y$	$-Y$	$+X$	$+Y$	$-X$	$+X$	$+Y$	$-X$	$-Y$
RLS	$+X$	$-X$	$+X$	$-X$	$-Y$	$+Y$	$-Y$	$+Y$	$-X$	$+X$	$-X$	$+X$	$+Y$	$-Y$	$+Y$	$-Y$

echo pulse sequence is

$$A_{\text{diff}}^{\text{ord}} = \frac{M_0}{2} \exp\left[-\gamma^2 G^2 D \tau_1^3 \left(\frac{2}{3} + \frac{\tau_2}{\tau_1}\right)\right] \quad (1)$$

where D is the diffusion coefficient defined by Einstein's law, $D =< z^2 > /2t$, in one dimension. The description is completed by considering also the T_1 and T_2 relaxation processes, and the total echo attenuation factor for ordinary diffusion is

$$A_{\text{diff,relax}}^{\text{ord}} = \frac{M_0}{2} \exp\left[-\gamma^2 G^2 D \tau_1^3 \left(\frac{2}{3} + \frac{\tau_2}{\tau_1}\right) - \frac{2\tau_1}{T_2} - \frac{\tau_2}{T_1}\right] \quad (2)$$

In the case of restricted diffusion, i.e. the hindrance of free propagation of the molecules due to geometric constraints such as pore walls, Einstein's law is replaced by a power law of the form $\langle z^2 \rangle = 2\alpha t^{\kappa}$, where α is the effective diffusion coefficient. The echo attenuation factor for restricted diffusion is known:[11,31]

$$A_{\text{diff}}^{\text{res}} = \frac{M_0}{2} \exp\left\{-6\frac{\alpha\gamma^2 G^2}{3(\kappa+1)(\kappa+2)}\left[\frac{1}{2}(2\tau_1 + \tau_2)^{\kappa+2} + \frac{1}{2}\tau_2^{\kappa+2} - (\tau_1 + \tau_2)^{\kappa+2} - \tau_1^{\kappa+2}\right]\right\} \quad (3)$$

In the case of $\kappa = 1$ and $\alpha = D$, Eqn (3) is equivalent to Eqn (1). Callaghan[13] and Stallmach *et al.*[14] have calculated the echo attenuation factors for anisotropic diffusion in pulsed gradients as

$$\left(A_{\text{diff}}^{\text{ani}}\right)_{\text{PFG}} = \frac{M_0}{2}\frac{1}{2}\int_0^{\pi} \exp\left[-\gamma^2\delta^2 G^2 \Delta (D_{||}\cos^2\theta + D_{\perp}\sin^2\theta)\right] \sin\theta \mathrm{d}\theta \quad (4)$$

where $D_{||}$ is the parallel and $D_{\perp}$ the perpendicular diffusion coefficient, δ is the gradient pulse width and Δ is the spacing between the two gradient pulses in the PFG experiment.

These results are easily adaptable to the description of anisotropic diffusion in steady gradients. Replacing the time-dependent part in Eqn (4) $\gamma^2\delta^2 G^2 \Delta$ by the appropriate terms for steady gradients according to Eqn (1) gives

$$\left(A_{\text{diff}}^{\text{ani}}\right)_{\text{SFG}} = \frac{M_0}{2}\frac{1}{2}\int_0^{\pi} \exp\left[-\gamma^2 G^2 \tau_1^3 \left(\frac{2}{3} + \frac{\tau_2}{\tau_1}\right)(D_{||}\cos^2\theta + D_{\perp}\sin^2\theta)\right] \sin\theta \mathrm{d}\theta \quad (5)$$

The fourth model, the coexistence of several differently fast diffusing phases, is a weighted superposition of the ordinary diffusion [Eqn (1)]. For example, in the case of two phases with two diffusion coefficients D_1 and D_2, and relative amounts p_1 and $p_2 = 1 - p_1$ of the two phases, the echo attenuation factor for the stimulated echo pulse sequence in a steady gradient is

$$A_{\text{diff}}^{\text{mul}} = \frac{M_0}{2}\left\{p_1 \exp\left[-\gamma^2 G^2 D_1 \tau_1^3 \left(\frac{2}{3} + \frac{\tau_2}{\tau_1}\right)\right] + p_2 \exp\left[-\gamma^2 G^2 D_2 \tau_1^3 \left(\frac{2}{3} + \frac{\tau_2}{\tau_1}\right)\right]\right\} \quad (6)$$

Equations (1), (3), (5) and (6) are used later to model the experimental echo attenuation factors.

EXPERIMENTAL

Experimental set-up

^{15}N magic angle spinning (MAS) NMR spectra were measured at room temperature and at −170 °C. The spectra were obtained by Fourier transformation of the FID, recorded after a 90° pulse at a MAS speed of 6 kHz under ^{1}H decoupling and a repetition time of 2 s at a field of 7 T, employing a Chemagnetics 6 mm double resonant MAS probe.

The ^{1}H SFG NMR measurements were performed on a Bruker 300/89 7 T superconducting magnet at a vertical displacement of $\Delta z = -23.15$ cm from the center of the magnet. At this point the magnetic field is $B_0 = 2.85$ T, corresponding to a proton resonance frequency $\omega_{\text{L}} = 2\pi \times 121.49$ MHz, which coincides with the ^{31}P NMR frequency at 7 T. Hence a standard ^{31}P probe could be used for the ^{1}H fringe field experiments. The precision of the vertical adjustment of the probe is better than $\Delta z = 35$ μm. The magnet was equipped with a pneumatic vibration damping system from Bruker. The magnetic field gradient was calibrated by comparison with literature data for water self-diffusion.[32] A value of $G = 39.70 \pm 0.53$ T m^{-1} was determined.

All stray field gradient measurements were carried out with the stimulated echo pulse sequence. The delay time τ_1 was set to a value of 20 μs and the delay time τ_2 was varied from 0.5 to 350 ms. From the length of the $\pi/2$ pulse (6 μs), a spectral excitation width of $\omega_{\text{FWHM}} = 2\pi \times 100.6$ kHz was estimated, corresponding to an excitation slice width of 58 μm. The width of the echo envelope is usually very narrow in high gradients and on the order of a few microseconds. Hence to record enough points to reduce the error in the integration of the echo intensity a sample rate of 5 MHz was used for the digitization of the echo signal.

The echo attenuation curves of the pyridine/MCM-41 samples were recorded with 2048 (samples B and C) and 4096 (sample A) accumulations for each point with a repetition time of 2 s. The bulk pyridine curve was recorded with 352 accumulations. Here the repetition time was chosen as 10 s (ca $1.25 \times T_1$, see below), which allows a faster repetition of the echo experiment, but gives a scaling of the echo amplitude. DC offset and phase distortion artifacts and signal contributions from the pulses were removed by appropriate phase cycling (Table 1) of the pulses.

For the evaluation of the diffusion data the ^{1}H longitudinal relaxation times T_1 in the magnetic field gradient at room temperature were measured independently by a saturation recovery experiment.

Preparation of mesoporous silica

The MCM-41 material was synthesized according to the method of Grün *et al.*[33] using cetyltrimethylammonium bromide (C_{16}TAB) as template. A 2.36 g amount of C_{16}TAB was dissolved in 120 g of water and the solution was mixed with 9.5 g of aqueous ammonia (25 wt%), then 10 g of

tetraethoxysilane (TEOS) were added under constant stirring at 35 °C. The precipitated product was kept in the reaction solution at 80 °C for 72 h and then filtered and washed with deionized water. After drying in air at 105 °C for 5 h, the product was heated to 550 °C at a rate of 1 K min^{-1} and calcined under flowing air.

NMR samples

For the SFG measurements, three samples of MCM-41 were loaded with pyridine at different filling factors: sample A, 64 mg MCM-41 + 15 µl pyridine, according to (25 ± 5)% pore volume; sample B, 61 mg MCM-41 + 30 µl pyridine, (55 ± 5)% sample C, 64 mg MCM-41 + 50 µl pyridine, (85 ± 5)%. The weight of the samples was controlled by microscales and the liquid pyridine added. As a reference, sample D containing bulk pyridine was prepared. For the ^{15}N NMR experiments sample E was prepared: ~10 mg of MCM-41 were dried at 400 K under high vacuum (~10^{-6} mbar) for 24 h and then 3 mg of dry ^{15}N-labeled pyridine (Chemotrade) [(30 ± 5)% pore volume] were condensed on to the sample. All tubes were sealed after preparation.

Sample characterization

As a first step, the mesoscopic structure and the porous properties of the MCM-41 material were characterized using x-ray diffraction (XRD) and gas adsorption. The small-angle XRD pattern (not shown) was recorded on a Kratky compact camera using Cu Kα radiation with an Ni filter in the range of 2θ angles from 0.5 to 6°. The diffraction pattern of the calcined MCM-41 sample exhibits four well-resolved peaks, indicating a two-dimensional hexagonal lattice (space group *P6mm*) with an interlattice spacing of $a = 4.5$ nm between the (100) planes. The nitrogen sorption isotherm at 77 K (Fig. 1) was measured by gas volumetry using a Gemini 2375 apparatus (Micromeritics). The BET surface area was 1040 m^2 g^{-1} and the specific pore volume was 0.93 cm^3 g^{-1}. The pore diameter $d = 3.3$ nm was calculated by the method of Dollimore and Heal.[34]

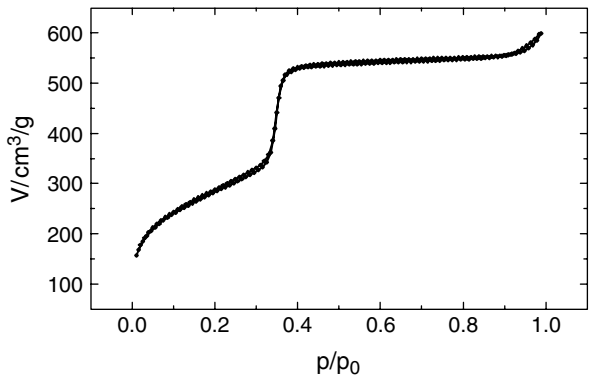

Figure 1. Nitrogen isotherm of the mesoporous silica MCM-41. From the absorption branch the specific (BET) surface area of the material ($S = 1040$ m^2 g^{-1}), the specific pore volume ($V_{pore} = 0.93$ cm^3 g^{-1}), and the pore diameter ($d = 3.3$ nm) were determined.

NMR data evaluation

The NMR data evaluation is based on Eqns (1), (3), (5) and (6), including the relaxation terms from Eqn (2). First, the echoes are numerically integrated in the time domain. For the simulation of the four diffusion models and the fitting of the experimental echo decay curves, the echo intensity data are fed into the laboratory-written Matlab program SIMECAT (SIMulation of ECho ATtenuation). According to the specific model, different parameter sets are used: ordinary diffusion is described with an isotropic diffusion coefficient D, whereas two-phase diffusion is described with two isotropic diffusion coefficients D_1 and D_2 and the corresponding relative amounts of the two phases p_1 and $p_2 = 1 - p_1$. The restricted diffusion echo decay is modeled by the two parameters of the power law [Eqn (3)], i.e. the effective diffusion coefficient α and the exponent of the power law κ. Finally, the anisotropic diffusion model is described by a parallel diffusion coefficient $D_{||}$ and a perpendicular diffusion coefficient $D_{\perp}$. In the case of anisotropic diffusion, the integral in Eqn (5) cannot be solved analytically, and a numerical integration has to be performed. This is done by summing over a grid of N equally spaced points in the interval $(0, \pi)$. Good convergence is reached with $N \geq 128$.

RESULTS AND DISCUSSION

NMR results

Three different samples (A, B, C) of pyridine confined in the mesopores of MCM-41 with filling factors of nominally 25, 55 and 85%, respectively, and a sample (D) of bulk pyridine as reference were studied by SFG NMR. Figure 2(a) displays the results of the stray field gradient stimulated echo attenuation curves of pyridine in the mesopores of MCM-41 and compares these data with those for bulk pyridine as reference. There are clear differences between the four curves, indicating different translational diffusion rates of the pyridine. In particular, the short-time diffusion rate of the pyridine in the mesopores increases with the filling factor, but is much lower than in bulk pyridine at long time.

For the evaluation of the diffusion data the ^1H longitudinal relaxation times T_1 of pyridine in the magnetic field gradient at room temperature were measured. For bulk pyridine a value of $T_1 = (7.9 \pm 0.4)$ s is determined in the fringe field. For the loaded silica samples values of $T_1 = (0.22 \pm 0.02)$ s (sample A, 25%), $T_1 = (0.46 \pm 0.04)$ s (sample B, 55%) and $T_1 = (0.52 \pm 0.04)$ s (sample C, 85%) are found.

Since the ^{15}N chemical shielding of the pyridine nitrogen is a very sensitive indicator of the hydrogen bonding situation, ^{15}N NMR measurements of the pyridine inside the mesopores at room temperature and at −170 °C (sample E) were performed in the next step. The spectra are shown in Fig. 3. At −170 °C two lines are observed, one at 276 and the other at 251 ppm. At room temperature, however, only a single line at a chemical shift of 267 ppm is observed.

Discussion

The analysis of the ^{15}N NMR spectra allows us to determine whether the pyridine molecules are in a single phase at room

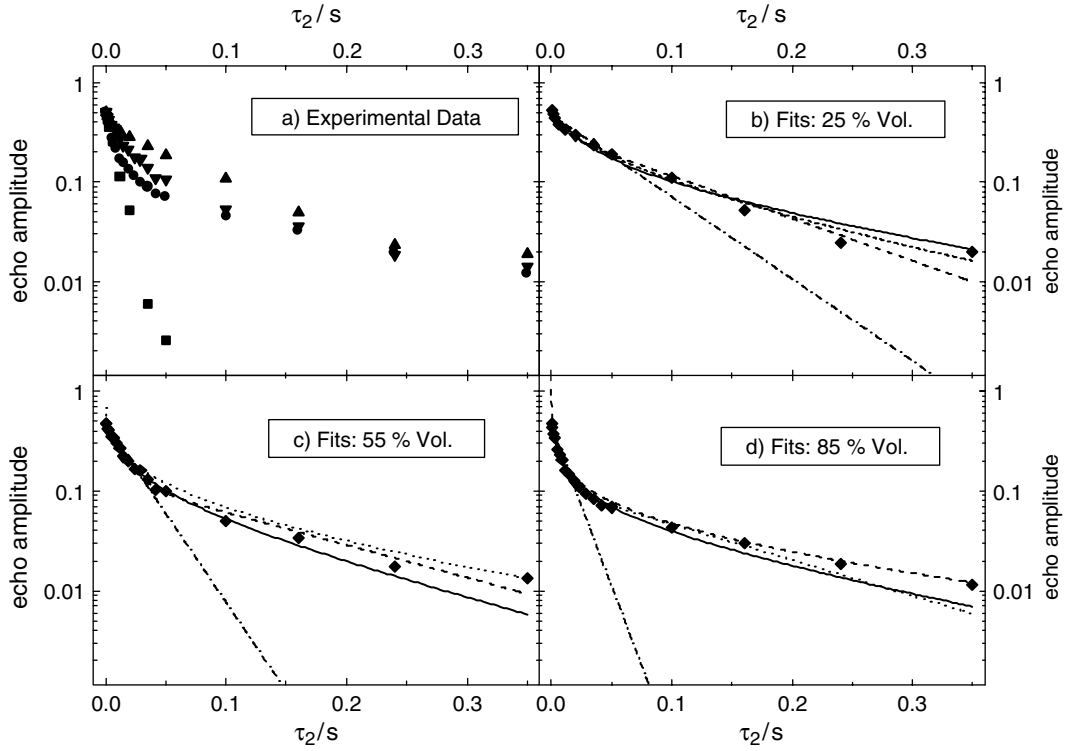

Figure 2. (a) Echo attenuation curves of pyridine in MCM-41 ($d = 3.3$ nm) for different filling levels: 25% (▲), 55% (▼) and 85% (●) pore volume. For comparison the bulk liquid pyridine data are also displayed (■). The echo intensities are normalized to $A(0) = 0.5$. Thus, the shape of the curves is directly comparable. (b)–(d) Fit results of pyridine in MCM-41 for different pore filling factors. The diamonds mark the experimental data and an estimated error of ±0.01 absolute amplitude. The fit curves are for ordinary diffusion (dash-dotted lines), restricted (dotted lines), anisotropic (dashed lines) and two-phase diffusion (solid lines).

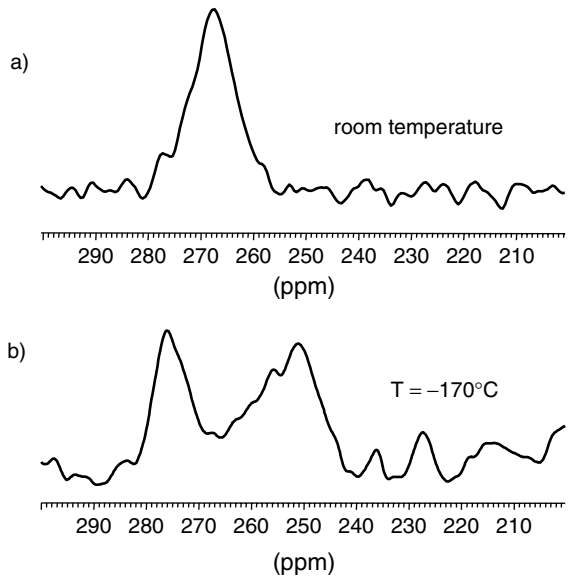

Figure 3. ^{1}H decoupled ^{15}N MAS NMR spectra (referenced to $^{15}NH_4Cl$) of 3 mg of dry ^{15}N-labeled pyridine confined in 10 mg of MCM-41 at (a) room temperature and (b) −170 °C. Note that only a single average line is present at room temperature, showing the equivalence of all pyridine molecules on the NMR time-scale.

temperature on the NMR time-scale, or whether there are two phases, one phase of molecules which are hydrogen-bonded to the surface, and a second phase of free pyridine molecules inside the pores. The two lines in the ^{15}N NMR spectra at low temperature prove that there are indeed two different species of pyridine molecules which do not exchange on the NMR time-scale. One line is close to the position of the chemical shift of bulk pyridine (276 ppm) and the other line (251 ppm) is at the typical value of pyridine bound to —SiOH groups (I. Shenderovich, A. Schreiber, E. Gedat, G. Buntkowsky, N. S. Golubev, G. H. Findenegg and H. H. Limbach in preparation).

At room temperature, however, only a single line is visible, which is the average of the two lines in the low-temperature spectrum. Hence it follows that at room temperature there is a fast exchange between the pyridine molecules on the pore surface and the pyridine molecules inside the pores and all pyridine molecules can be considered as a single phase on the NMR time-scale.

From the ^{1}H NMR experiments, the translational diffusion motions of the pyridine inside the mesopores are elucidated as follows. Both echo attenuation and T_1 relaxation times exhibit a strong dependence on the filling factor. From the ^{15}N spectra, it is evident that at room temperature all pyridine molecules are in fast exchange on a time-scale of milliseconds, which is also the relevant time-scale of the T_1 and diffusion measurements. The spin–lattice relaxation rates for pyridine on the surface and pyridine in the pore volume are in general different and the filling factor dependence of the spin–lattice relaxation rate is a direct consequence of the fast exchange between the surface phase and inner pyridine molecules: as the most simple model the measured T_1

time is the weighted average of the rates corresponding to the two phases.

The question now arises of what the origin of the filling factor-dependent changes of the diffusion rate is. As discussed in the Introduction, there are several different diffusion models, namely ordinary diffusion, a multi-phase model, where different separate phases are present inside the pores; a restricted diffusion model, which explains the differences as the result of the finite size of the pores; and finally the model of anisotropic diffusion, which explains the differences as the result of the strongly anisotropic geometry of the pores. The least-squares fit parameters from the SIMECAT fit of these models are given in Table 2 and the fit curves are displayed in Fig. 2(b), (c) and (d) for samples A, B and C, respectively. From the figures it is evident that at long diffusion times there are strong deviations between the experimental and the calculated data for the ordinary diffusion model. Hence ordinary isotropic diffusion can be excluded for the diffusion of pyridine inside the mesopores. All three other diffusion models are able to reproduce the experimental data. To decide further between these models one has to investigate the resulting key parameters (Table 2) obtained from the fits (note that in principle it is possible to exploit the different τ_1 dependences of the diffusion models in addition to the τ_2 dependence to distinguish between the models. However, short T_2 relaxation times can strongly obscure this dependence. Therefore we decided to not perform a variation of τ_1).

Table 2. Fit results of the SFG measurements of pyridine in MCM-41 for different pore filling factors and for the four diffusion models: (i) ordinary, (ii) restricted, (iii) anisotropic and (iv) two-phase diffusion[a]

Model	Parameter	25%	55%	85%
Ordinary	D (m^2 s^{-1})	2.3×10^{-10}	5.1×10^{-10}	9.5×10^{-10}
	χ^2	0.00464	0.01190	0.02691
Restricted	α(m^2 $s^{-\kappa}$)	7.6×10^{-11}	6.8×10^{-11}	7.9×10^{-11}
	κ	0.62	0.32	0.14
	χ^2	0.00061	0.00390	0.00101
Anisotropic	$D_{\|\|}$ (m^2 s^{-1})	1.0×10^{-9}	2.7×10^{-9}	6.8×10^{-9}
	$D_\perp$ (m^2 s^{-1})	2.2×10^{-11}	5.4×10^{-11}	3.5×10^{-11}
	χ^2	0.00019	0.00116	0.00069
Two phases	D_1 (m^2 s^{-1})	5.0×10^{-10}	1.0×10^{-9}	2.0×10^{-9}
	p_1	0.60	0.73	0.77
	D_2 (m^2 s^{-1})	5.0×10^{-11}	7.0×10^{-11}	8.3×10^{-11}
	p_2	0.40	0.27	0.23
	χ^2	0.00024	0.00148	0.00127

[a] D is the isotropic diffusion coefficient, α the effective diffusion coefficient for restricted diffusion, κ is the exponent of the power law, $D_{||}$ and $D_\perp$ are the parallel and perpendicular diffusion coefficient, respectively. D_1 and D_2 are the two diffusion coefficients for two-phases diffusion, p_1 and p_2 are the corresponding relative amounts of the two phases and $\chi^2 = \sum_k \left(A_{\text{exp}} - A_{\text{calc}}\right)^2$ is the quadratic deviation between calculated and experimental normalized decay curve.

The multi-phase model is based on a superposition of several decay curves with different decay constants, resulting in a multi-exponential decay curve. From the preparation it is evident that all pyridine molecules are inside the pores and that the pores exhibit a very high degree of homogeneity regarding their diameters. Hence one can assume that there are no domains with different diffusion coefficients, which would lead to a simple superposition of different decay curves from these domains. The only remaining possible difference between pyridine molecules is their distance from the pore surface. This, however, would imply that pyridine molecules with different distances from the pore wall have different diffusion coefficients, but, as discussed above, the ^{15}N measurements show that at room temperature all pyridine molecules are in fast exchange already on a time-scale below 1 ms, because the pore diameter corresponds to only a few pyridine diameters (see Fig. 6). Hence at room temperature only a single average decay constant on the time-scale of the diffusion experiment is expected. This would cause a mono-exponential decay of the echo, which is in clear contradiction to the experimental result. Hence a multi-phase model seems to be very improbable as the origin of the observed dependence.

In the next step, the restricted diffusion model is considered. Restricted diffusion is characterized by an effective diffusion coefficient α and a power law with exponent κ for the time dependence [Eqn (3)]. The results are shown in Fig. 2(b), (c) and (d). The fits for the three samples give the same effective diffusion coefficient of $\alpha = (7.4 \pm 1.0) \times 10^{-11}\ m^2\ s^{-1}$, but with significantly different exponents, namely $\kappa = 0.62$ for a filling factor of 25%, $\kappa = 0.32$ for 55% and $\kappa = 0.14$ for 85% (see Table 2). This indicates an increasing restriction with higher filling levels, implying a mutual hindrance of the guest molecules that grows with the concentration. In principle one could rationalize such an increase of the mutual hindrance as the result of the reduction of the mean free pathway by the increase in the concentration. To study this model, the time dependence of the root mean square displacement $r = \sqrt{\alpha t^\kappa}$, according to the modified Einstein relation for restricted diffusion, is plotted in Fig. 4. The long time evolution of the graphs is in good agreement with the model of restricting geometry, because for smaller exponents κ the graphs are closer to the asymptotic value of the r.m.s. displacement and grow very slowly. At short times, however, the curves approach a step function in the limit and become singular with decreasing value of κ. This implies a very fast initial diffusion which then becomes very slow. Such a behavior is incompatible with the assumed increase in the mutual hindrance of the molecules. Hence the restricted diffusion seems to be very improbable as the origin of the observed dependence.

In the last step the anisotropic diffusion model is discussed. In contrast to the models of restricted and multi-phase diffusion, this model is in agreement with all experimental parameters. We therefore conclude that it is the most probable origin of the observed dependence of the decay curves. From the fits of the data shown in Fig. 2 for the three samples A, B and C, diffusion coefficients

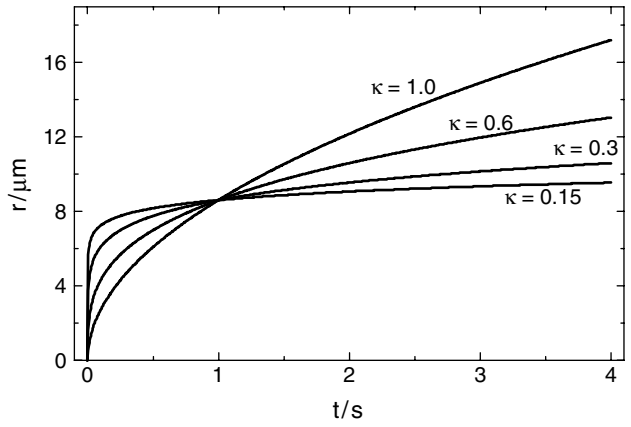

Figure 4. Theoretical mean displacement according to Einstein's equation ($D = \langle r^2 \rangle / t^{\kappa}$) for the parameters derived by a fit of the experimental data with Eqn (3). The average value $\alpha = 7.4 \times 10^{-11}$ is used. The graphs are displayed for the three different κ values, according to the fit results for restricted diffusion, and, for comparison, for $\kappa = 1$ (ordinary diffusion).

parallel to the pores' cylinder axes of $D_{||} = (1.0, 2.7, 6.8) \times 10^{-9}$ m^2 s^{-1} and diffusion coefficients perpendicular to the pores' axes $D_{\perp} = (2.2, 5.4, 3.5) \times 10^{-11}$ m^2 s^{-1} are found (see Table 2). These values indicate a growth of the parallel diffusion coefficient when increasing the filling factor. The perpendicular diffusion coefficient, however, is practically independent of the filling factor. The growth of the parallel diffusion coefficient can be understood by the following model. As discussed in the introduction, the pyridine molecules have a strong tendency to form hydrogen bonds with surface —SiOH groups. As a consequence, the first adsorption layer of pyridine in the pores consists of those pyridine molecules which are hydrogen bond to surface OH groups. To estimate the amount of pyridine in this first layer, one needs to know the surface density of —SiOH groups. This surface density has been determined from surface coating experiments by Anwander *et al*.[35] as 1.85 nm^{-2} and by Zhao and Lu[36] as 1.9 nm^{-2} at a maximum coverage (85%). Assuming that the density of pyridine in the pores is approximately the same as the density of bulk liquid pyridine, the volume V_{mol} of a single pyridine molecule in the pores is $V_{\mathrm{Mol}} = M_{\mathrm{M}}/(N_{\mathrm{A}}\rho) = (0.5\,\mathrm{nm})^3$, where M_{M} is the molar mass and ρ the density of pyridine in the liquid state. If S is the specific (BET) surface area, the number of molecules on the surface of 1 g of MCM-41 can be estimated as $N = S \times (1.85/\mathrm{nm}^2)$ and the relative volume as $V/V_{\mathrm{pore}} = N \times (0.5\,\mathrm{nm})^3/V_{\mathrm{pore}}$. Thus the relative volume of the first layer is

$$\left(\frac{V}{V_{\mathrm{pore}}}\right)_{\mathrm{1stlayer}} = \frac{S \times 1.85/\mathrm{nm}^2 \times M_{\mathrm{M}}}{\rho \times N_{\mathrm{A}} \times V_{\mathrm{pore}}} \qquad (8)$$

This relative volume of the first layer was calculated for three individual MCM-41 materials ($d = 2.9$ nm; $d = 3.3$ nm; $d = 3.7$ nm) with different pore diameters to 35, 26 and 18%, respectively, (circles in Fig. 5) and linearly extrapolated for other diameters. For the inner pyridine molecules we have assumed for simplicity that with increase in the concentration subsequent inner layers are filled. Note that, except for the first layer, the model of subsequent adsorption of monolayers in not unique: in principle, there could be a free gas phase of pyridine molecules inside the pores. However, the nitrogen isotherm (Fig. 1) that shows pore condensation at a relative pressure of $p/p_0 = 0.35$ renders this very unlikely. Thus one can assume that the excess pyridine molecules in the inner pore volume are in a liquid phase. It is possible, however, that these molecules form small droplets or large domains across the whole cross-section of a part of the pores. From our experiments it is impossible to decide between these alternatives. For the estimation of the relative number of molecules in the surface monolayer and in the pore volume, this is not critical. The relative volumes of the first three adsorption layers of pyridine in cylindrical pores and pore diameters between 2.7 and 3.9 nm are calculated and displayed in Fig. 5.

From this calculation, it follows that all pyridine molecules of the 25% filled sample A are in the first layer, i.e. hydrogen bonded to the surface. Hence their diffusion is a pure surface diffusion. This explains why their parallel diffusion coefficient of $D_{||} = 1.0 \times 10^{-9}$ m^2 s^{-1} is smaller than the diffusion coefficient in bulk pyridine ($D_{\mathrm{bulk}} = 1.6 \times 10^{-9}$ m^2 s^{-1}): this decrease of the parallel diffusion coefficient is a result of the strong hydrogen bond interaction between surface —SiOH groups and pyridine N sites, which exceeds mutual pyridine molecule interaction. Bernstein and Pfeifer calculated for the OH···N hydrogen bridge of the adsorption complex pyridine–OH group at the surface of silica a stabilization energy of ca 50 kJ mol^{-1},[37] which is approximately the activation energy of the diffusion for these molecules. When the filling factor is increased the parallel diffusion coefficient grows and for the 55% filled sample (B) the parallel diffusion coefficient of $D_{||} = 2.7 \times 10^{-9}$ m^2 s^{-1}, exceeds both the parallel diffusion coefficient of the 25% filled sample and the bulk diffusion coefficient. As shown in Fig. 5 the second layer starts to grow

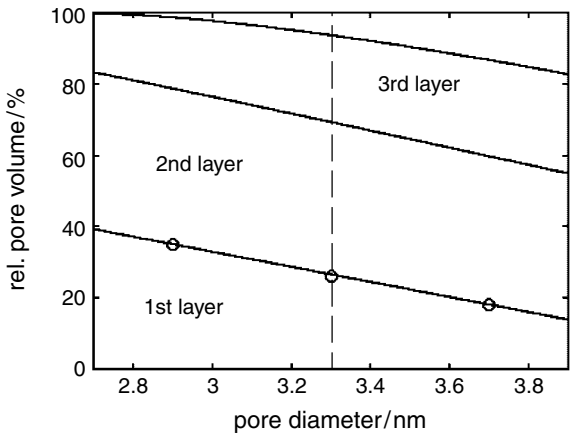

Figure 5. Volume of the first three adsorption layers of pyridine [$V_{\mathrm{molecule}} = (0.5\,\mathrm{nm})^3$] in pores with different diameters, as calculated with a model described in the text. The three solid lines mark the boundaries between the neighboring layers. The three circles are calculated from real materials as described in the text, and the vertical line stresses the pore diameter of 3.3 nm.

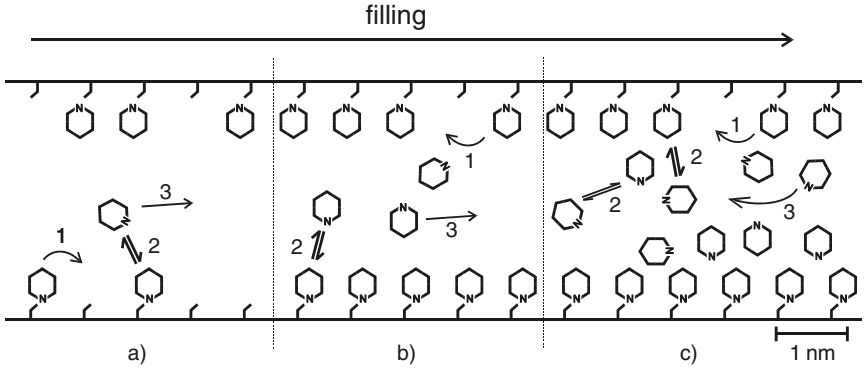

Figure 6. Diffusion model of pyridine in MCM-41. The plot is scaled according to the scale bar in the bottom right corner. The top and bottom lines represent the pore walls and the 'hooks' on them represent surface OH groups. Pyridine molecules at increasing filling levels (a)–(c) are either adsorbed on the surface OH groups or diffuse in the pore volume. Three different diffusion processes are distinguished: (1) surface diffusion (jump motion over the OH groups), (2) adsorption and desorption processes and (3) 'free' diffusion.

at a filling factor of ca 30%. In sample B (55%) the second layer is already more than half full and consequently at any time an appreciable number of guest molecules in sample B are not hydrogen bonded to the surface. This has two consequences, both of which tend to increase the diffusion coefficient: on the one hand, pyridine molecules in this second layer need no activation energy for breaking the hydrogen bonds to surface —SiOH groups, and on the other hand, because of the partial filling, they have a larger free volume than a pyridine molecule in bulk pyridine. As discussed above, all pyridine molecules are in fast exchange on the time-scale of diffusion and behave as a single phase. This implies that here the diffusion of the pyridine molecules is mediated via the exchange of a surface pyridine and a pyridine molecule in the second layer. The rate-determining step for the diffusion of the molecules is the exchange rate between surface and inner pyridine molecules and the diffusion rate is the weighted average of the diffusion rates of surface and inner molecules. A true-to-scale sketch of these mechanisms is shown Fig. 6. Here, three different diffusion processes are distinguished: (1) surface diffusion by jump motion from one OH group to another, (2) absorption/desorption processes from and to the surface and from and to the inner pore volume and (3) quasi-free diffusion in the pore volume. Processes 1 and 3 result in an average parallel diffusion coefficient, which depends on the filling level, as indicated by the sections a, b and c in Fig. 6. Process 2 mediates the exchange between the different areas.

In the 85% filled sample finally the third layer is already partially filled and the parallel diffusion coefficient grows again. This further increase can be mainly attributed to the higher number of fast-diffusing molecules, which shifts the average diffusion coefficient towards faster rates. From the absolute value, which is now about four times larger than the diffusion coefficient of the bulk liquid, one can assume that besides the larger free volume of pyridine molecules inside the mesopores there is also a second reason for the fast parallel diffusion, namely the reduction of the dimensionality from three dimensions in bulk pyridine to one dimension in the mesopores. This faster diffusion in the pores than in the bulk is analogous to the well known lowering of the melting-point of liquids in mesopores, which was observed, for example, for water in MCM-41.[38,39]

The perpendicular diffusion coefficient, in contrast, is independent of the filling factor within the margin of error. The arithmetic mean of the three values of the perpendicular diffusion coefficient in the three samples is $D_\perp = 3.7 \times 10^{-11}\ m^2\ s^{-1}$. The fit results of the parallel diffusion coefficient hardly change with the assumption of the average perpendicular diffusion coefficient. As discussed by Stallmach *et al*.,[14] the fact of non-zero perpendicular diffusion coefficient in mesopores is attributed to residual interconnectivity of the parallel pores and/or to non-negligible bending of the pores. Hence $D_\perp$ can be considered as a material constant and should therefore be the same for all filling factors.

CONCLUSION

We have found the following microscopic picture for the diffusion of pyridine in the mesoporous silica MCM-41 from the combination of ^{15}N MAS NMR spectroscopy, ^1H T_1 relaxation measurements and ^1H SFG NMR diffusometry: the model of anisotropic diffusion of a single phase of pyridine molecules is in agreement with all experimental parameters and gives a good description of the diffusion of pyridine molecules in mesoporous silica at room temperature. This anisotropy is the result of the geometric structure of the pores. The perpendicular diffusion is mainly the result of the permeability of the pore walls. The rate of the parallel diffusion depends strongly on the filling factor. If only a monolayer of pyridine molecules is on the surface, the diffusion rate is lowered, because of the hydrogen bonding of these molecules to the surface. If the filling factor is increased, subsequent inner layers are populated. The fast exchange between these inner layers and the surface layer leads to a strong increase in the diffusion coefficient, which for large filling factors exceeds the rate of bulk pyridine. This faster diffusion can be attributed to two reasons, a larger free volume of the individual pyridine molecule and the reduced dimensionality of the diffusion process.

Finally, we note that these surface effects influence not only the translational but also the rotational degrees of freedom of guest molecules, as was shown recently by low-temperature ^{2}H NMR spectroscopy (E. Gedat, A. Schreiber, J. Albrecht, I. Shenderovich, G. Findenegg, H. H Limbach and G. Buntkowsky. *J. Phys. Chem*. submitted).

ACKNOWLEDGEMENT

This work was supported by the Deutsche Forschungsgemeinschaft in the framework of the Sonderforschungsbereich 448 'Mesoskopisch Strukturierte Verbundsysteme.'

REFERENCES

1. Kapur GS, Cabrita EJ, Berger S. *Tetrahedron Lett.* 2000; **41**: 7181.
2. Hansen PE, Simon S. *Magn. Reson. Chem.* 1997; **35**: 320.
3. Tjandra N, Bax A. *J. Am. Chem. Soc.* 1997; **119**: 8076.
4. Ciesla U, Schüth F. *Microporous Mesoporous Mater.* 1999; **27**: 131.
5. Beck JS, Vartuli JC, Roth WJ, Leonowicz ME, Kresge CT, Schmitt KD, Chu CT-W, Olson DH, Sheppard EW, McCullen SB, Higgins JB, Schlenker JL. *J. Am. Chem. Soc.* 1992; **114**: 10 834.
6. Zhao D, Feng J, Huo Q, Melosh N, Fredrickson GH, Chmelka BF, Stucky GD. *Science* 1998; **279**: 548.
7. Kärger J, Ruthven DM. *Diffusion in Zeolites and Other Microporous Solids*. Wiley: New York, 1992.
8. Keil FJ, Krishna R, Coppens M-O. *Rev. Chem. Eng.* 2000; **16**: 71.
9. Hahn EL. *Phys. Rev.* 1950; **80**: 580–594.
10. Woessner DE. *J. Chem. Phys.* 1961; **34**: 2057–2061.
11. Kimmich R. *NMR Tomography Diffusometry Relaxometry*. Springer: Berlin, 1997.
12. Kärger J, Bär N-K, Heink W, Pfeifer H, Seiffert G. *Z. Naturforsch, Teil A.* 1994; **50**: 186.
13. Callaghan PT. *Principles of Nuclear Magnetic Resonance Microscopy*. Clarendon Press: Oxford, 1991.
14. Stallmach F, Kärger J, Krause C, Jeschke M, Oberhagemann U. *J. Am. Chem. Soc.* 2000; **122**: 9237–9242.
15. Hansen EW, Schmidt R, Stöcker M. *J. Phys. Chem.* 1996; **100**: 11 396.
16. Menzel MI, Han S-I, Stapf S, Blümich B. *J. Magn. Reson.* 2000; **143**: 376–381.
17. Kimmich R, Weber HW. *Phys. Rev. B* 1993; **47**: 788.
18. Kimmich R, Klammler F, Skirda VD, Serebrennikova IA, Maklakhov AI, Fatkullin N. *Appl. Magn. Reson.* 1993; **4**: 425.
19. Bodurka J, Gutsze A, Buntkowsky G, Limbach H-H. *Z. Chem. Phys.* 1995; **190**: 99.
20. Bodurka J, Buntkowsky G, Gutsze A, Limbach H-H. *Z. Naturforsch., Teil C* 1996; **51**: 81.
21. Bodurka J, Buntkowsky G, Gutsze A, Limbach H-H. *Appl. Spectrosc.* 1996; **50**: 1421.
22. Gutsze A, Bodurka J, Olechnowicz R, Buntkowsky G, Limbach H-H. *Z. Naturforsch., Teil C*. 1995; **50**: 410.
23. Pyckhout W, Horemans N, Alsenoy CV, Geise J, Rankin DWH. *J. Mol. Struct.* 1987; **156**: 315.
24. Appel M, Fleischer G, Kärger J, Fujara F, Chang I. *Macromolecules* 1994; **27**: 4274.
25. Fleischer G, Fujara F. *Macromolecules* 1992; **25**: 4210.
26. Kimmich R, Unrath W, Schnur G, Rommel E. *J. Magn. Reson.* 1991; **91**: 136–140.
27. Kimmich R, Zavada T, Stapf S. *Mater. Res. Soc. Symp. Proc.* 1997; **464**: 313.
28. Ylihautala M, Jokisaari J, Fischer E, Kimmich R. *Phys. Rev. E* 1998; **57**: 6844.
29. Pahl S, Fleischer G, Fujara F, Geil B. *Macromolecules* 1997; **30**: 1414.
30. Chang I, Fujara F, Geil B, Hinze G, Sillescu H, Tölle A. *J. Non-Crystalline Solids* 1994; **172–174**: 674.
31. Kärger J, Heitjans P, Haberlandt R. *Diffusion in Condensed Matter*. Vieweg: Braunschweig, 1998.
32. Tofts PS, Lloyd D, Clark CA, Barker GJ, Parker GJM, McConville P, Baldock C, Pope JM. *Magn. Reson. Med.* 2000; **43**: 368.
33. (a) Grün M, Unger KK, Matsumoto A, Tsutsumi K. *Characterization of porous solids IV*, McEnaney B, Mays TJ, Roquérol J, Rodriguez-Reinoso F, Sing KSW, Unger KK (eds). The Royal Society of Chemistry: Cambridge, 1997; 81–89; (b) Grün M, Unger KK, Matsumoto A, Tsutsumi K. *Microporous and Mesoporous Materials* 1999; **27**: 207.
34. Dollimore D, Heal GR. *J. Appl. Chem.* 1964; **14**: 109.
35. Anwander R, Nagl I, Widenmayer M, Engelhardt G, Groeger O, Palm C, Röser T. *J. Phys. Chem. B* 2000; **104**: 3532.
36. Zhao XS, Lu GQ. *J. Chem. Phys.* 1998; **102**: 1556.
37. Bernstein T, Pfeifer HZ. *Phys. Chem.* 1985; **266**: 94–100.
38. Hansen EW, Stöcker M, Schmidt R. *J. Phys. Chem.* 1996; **100**: 2195–2200.
39. Schreiber A, Ketelsen I, Findenegg GH. *Phys. Chem. Chem. Phys.* 2001; **3**: 1185.